Article

Dynamical criticality of spin-shear coupling in van der Waals antiferromagnets

Faran Zhou[1], Kyle Hwangbo[2], Qi Zhang [1,2,9], Chong Wang [3], Lingnan Shen[2], Jiawei Zhang[1], Qianni Jiang[2], Alfred Zong [4], Yifan Su[5], Marc Zajac [1], Youngjun Ahn[1,6], Donald A. Walko[1], Richard D. Schaller [7], Jiun-Haw Chu [2], Nuh Gedik [5], Xiaodong Xu [2,3], Di Xiao [2,3] & Haidan Wen [1,8] ✉

The interplay between a multitude of electronic, spin, and lattice degrees of freedom underlies the complex phase diagrams of quantum materials. Layer stacking in van der Waals (vdW) heterostructures is responsible for exotic electronic and magnetic properties, which inspires stacking control of two-dimensional magnetism. Beyond the interplay between stacking order and interlayer magnetism, we discover a spin-shear coupling mechanism in which a subtle shear of the atomic layers can have a profound effect on the intralayer magnetic order in a family of vdW antiferromagnets. Using time-resolved X-ray diffraction and optical linear dichroism measurements, interlayer shear is identified as the primary structural degree of freedom that couples with magnetic order. The recovery times of both shear and magnetic order upon optical excitation diverge at the magnetic ordering temperature with the same critical exponent. The time-dependent Ginzburg-Landau theory shows that this concurrent critical slowing down arises from a linear coupling of the interlayer shear to the magnetic order, which is dictated by the broken mirror symmetry intrinsic to the monoclinic stacking. Our results highlight the importance of interlayer shear in ultrafast control of magnetic order via spin-mechanical coupling.

Understanding spin–lattice coupling is essential for deriving new control schemes of coupled degrees of freedom in quantum materials. In vdW materials, the unique spin–lattice coupling different from the three-dimensional system can lead to exotic electronic[1–4], magnetic[5–11], and mechanical[12,13] functionalities. Previous studies have shown that engineering structural configurations such as stacking order[14,15], interlayer twist angle[16], and strain states[17–20] can effectively control the interlayer magnetic coupling[15,21,22], thus tuning the interlayer magnetic orders. But the structural control of the intralayer magnetism can be challenging because the intralayer magnetic order is robust against small in-plane strain[23]. Enabling interlayer structural control of intra-layer magnetism can expand the existing heterostructure engineering for controlling magnetism in all dimensions on demand, calling for a new spin–lattice coupling mechanism.

Here, we report that the shear motion of the atomic layers strongly couples to the intralayer magnetism, a phenomenon that is rooted in the unique structural anisotropy and magnetic symmetry of vdW materials. The interlayer shear, a degree of freedom that was largely overlooked due to the weak vdW interaction, turns out to play a critical role in determining the spin orders in individual layers. Our

[1]X-ray Science Division, Argonne National Laboratory, Lemont, IL, USA. [2]Department of Physics, University of Washington, Seattle, WA, USA. [3]Department of Materials Science and Engineering, University of Washington, Seattle, WA, USA. [4]Department of Chemistry, University of California Berkeley, Berkeley, CA, USA. [5]Department of Physics, Massachusetts Institute of Technology, Cambridge, MA, USA. [6]Department of Materials Science and Engineering, University of Wisconsin-Madison, Madison, WI, USA. [7]Center for Nanoscale Materials, Argonne National Laboratory, Lemont, IL, USA. [8]Materials Science Division, Argonne National Laboratory, Lemont, IL, USA. [9]Present address: Department of Physics, Nanjing University, Nanjing, China. ✉e-mail: wen@anl.gov
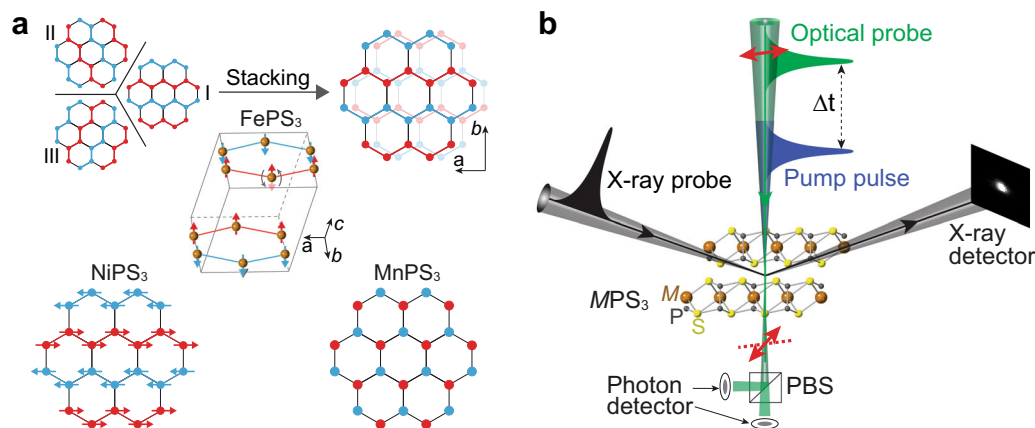
Fig. 1 | vdW antiferromagnetic (AFM) materials and ultrafast measurements.
a Top row: cartoons depict that the energy degeneracy of three intralayer zigzag antiferromagnetic orders is lifted by monoclinic stacking in $FePS_3$ so that the zigzag chain is stabilized along the monoclinic stacking direction. Red and blue dots represent up and down spin with respect to the basal plane. The cartoon in the middle row shows the three-dimensional unit cell of $FePS_3$, where only the Fe atoms are drawn. The curved gray arrows indicate the spin-flip fluctuations at random Fe atom sites close to T_N. Bottom row: magnetic structure of zigzag AFM in $NiPS_3$ and Néel-type AFM in $MnPS_3$. **b** Time-resolved multimodal measurements of optically excited vdW antiferromagnets. The X-ray diffraction directly characterizes the lattice configuration, while the optical transmission linear dichroism measures the intralayer AFM order. The red arrow indicates the polarization rotation of the optical probe light pulse. PBS: polarizing beam splitter.

studies focus on a family of isostructural vdW antiferromagnets, MPS_3 (M: Fe, Ni, Mn)[24], which have monoclinic structures in the space group of C2/m with a monoclinic angle $\beta = 107.2°$. Below the Néel temperature (T_N), bulk $FePS_3$ and $NiPS_3$ exhibit the zigzag AFM order along the a axis[25] while $MnPS_3$ exhibits the Néel-type AFM order (Fig. 1a). Although optical probes such as Raman spectroscopy[26–29] and second harmonic generation[30,31] have been applied to detect the local structural symmetry, a direct structural probe of long-range lattice configuration with atomistic accuracy is needed to understand the impact of crystallographic configurations on magnetic ordering quantitatively. Early equilibrium structural characterization has shown that multiple lattice degrees of freedom exhibit abrupt changes concurrently with the magnetic ordering temperature in $FePS_3$[32]. However, it is not yet clear whether there is a primary structural parameter that couples with intralayer magnetism and how this lattice configuration influences the magnetism.

Results

### Correlated critical slowing down of the interlayer shear and intralayer magnetic order

To disentangle the complex coupling between multiple lattice degrees of freedom and magnetic orders in MPS_3, we drove the samples into nonequilibrium states by optical excitation and quantitatively tracked the structural and spin dynamics by X-ray diffraction (XRD) and transient optical linear dichroism (OLD), respectively (Fig. 1b). Time-resolved high-resolution XRD measurements were performed at the 7ID-C beamline of the Advanced Photon Source (see Methods). Three Bragg peaks (002, $\bar{2}$02, 0$\bar{2}$2) of $FePS_3$ were measured as a function of time to reconstruct the dynamics of its unit cell (Fig. 2a). At the sample temperature of 95 K, below T_N of 117 K, we discovered that the 002 peak shifted $\Delta q = 0.0098\,Å^{-1}$ toward the $-\mathbf{c}^*$ direction at 5 ns (Supplementary Note 1 and Fig. 2b) as a result of an interlayer expansion upon optical excitation. This is consistent with an increase in lattice temperature by about 30 K (see Supplementary Note 2). Consequently, the interlayer expansion relaxed on the 200 ns time scale as the sample cooled down. This thermal recovery time increased as a function of temperature and peaked at 110 K. The magnitude and the peak temperature of this slowing down were reproduced using a thermal relaxation model involving the latent heat, as described in Supplementary Note 2.

Unlike the 002 peak that shifts toward the $-\mathbf{c}^*$ direction, the $\bar{2}$02 peak shifted to the opposite direction ($+\mathbf{c}^*$) at sample temperatures below T_N. As shown in the schematic of the reciprocal space (Fig. 2a), the green and red parallelograms represent the unit cell in the ac plane before and after the laser excitation, respectively. The opposite shifts of 002 and $\bar{2}$02 peak correspond to a decrease in the monoclinic angle β (Fig. 2a), i.e., there is an interlayer shear along the a axis after laser excitation. The dynamics measured at the $\bar{2}$02 peak (Fig. 2c) can be modeled by two simultaneous relaxation processes. One is the thermal relaxation that can be approximated by an exponential decay of the peak shift toward the $-\mathbf{c}^*$ direction. The other is the relaxation of the interlayer shear, which is proportional to the change of the monoclinic angle β after the excitation as defined by $\Delta\beta(t) = \beta(t) - \beta(t < 0)$ (Fig. 2d and Supplementary Note 3). The relaxation of $\Delta\beta$ can be approximated by an exponential decay of the peak shift to the $+\mathbf{c}^*$ direction. Therefore, a bi-exponential function fits the dynamics of the $\bar{2}$02 peak (solid lines in Fig. 2c and see Supplementary Note 4).

A striking observation is that the recovery time of β is significantly longer than the thermal relaxation process measured by the 002 peak (Fig. 2e). The time constant of its recovery τ_β diverges at 116 ± 2 K, two orders of magnitude larger than the recovery time measured at 70 K. The error bar of the critical temperature represents uncertainties in determining the sample temperature under laser illumination. This critical temperature coincides with T_N (117 K), indicating a strong correlation between the interlayer shear and the antiferromagnetic-to-paramagnetic phase transition. The relaxations of the interlayer shear along the b axis (angle α, measured by 0$\bar{2}$2 and 002 Bragg peaks) as well as the lattice parameters a and b (Supplementary Fig. 3) did not exhibit such critical slowing down. Therefore, the monoclinic angle β is the only structural parameter of the unit cell that exhibits critical slowing down at T_N.

The divergence in the recovery time of the interlayer shear at the magnetic ordering temperature indicates a correlation of lattice shear with the spin order. To investigate the dynamics of the spin order, we performed time-resolved OLD measurements via transient absorption in a transmission geometry (Fig. 1b). The intralayer anisotropic optical absorption along and perpendicular to the zigzag spin chains results in a polarization rotation (φ_{LD}) of the linearly polarized optical probe beam. The change of polarization rotation ($\Delta\varphi_{LD}$) of the optical probe beam measures the dynamics of the intralayer zigzag AFM order[33,34]. To capture the recovery dynamics, we employed an asynchronous optical sampling technique (see "Methods") which extended the measurement time window to microsecond scales and thus allowed us
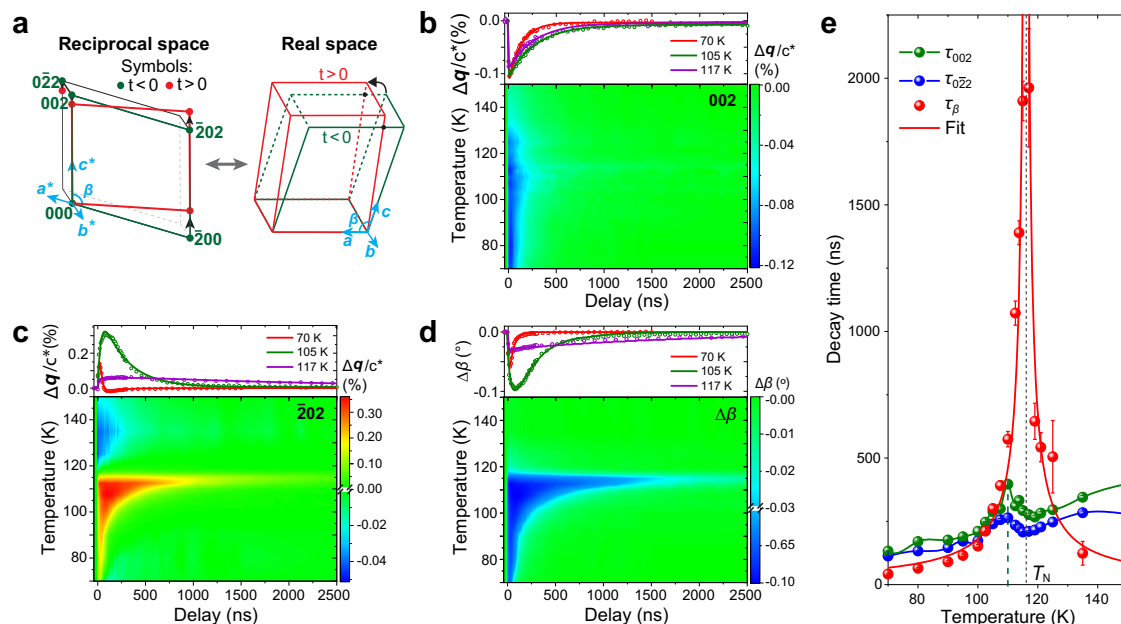
Fig. 2 | Temperature-dependent structural dynamics in FePS$_3$. a Schematics of the reciprocal- and real-space unit cell before (green dots and lines) and after (red dots and lines) laser excitation. **b** Dynamics of the 002 peak shift ($\Delta\boldsymbol{q}$) along the **c*** direction as a function of the temperature. **c** Dynamics of the $\bar{2}02$ peak shift as a function of the temperature. **d** Dynamics of β change ($\Delta\beta$) as a function of temperature. Top panels in (**b**−**d**) are the line cuts of three representative temperatures, in which the solid lines represent the fitting results (see text). **e** Relaxation time of the 002, $0\bar{2}2$ peak shifts, and $\Delta\beta$ across T_N. τ_β was fitted by a power-law function detailed in Supplementary Note 5. The vertical green dashed line at 110 K indicates the peak of the thermal relaxation time. The error bars represent the standard deviation of exponential fitting detailed in Supplementary Note 4.

to accurately extract the relaxation time and the critical exponent. This time scale is otherwise challenging to access due to the limited time window of a few nanoseconds probed in an earlier study[33]. We found that the recovery time of the intralayer zigzag AFM order (τ_{LD}) varies more than one order of magnitude as a function of temperature and diverges at 115 ± 2 K (Fig. 3a, b), indicating strong intralayer spin fluctuations at T_N.

The relaxation time of the interlayer shear (τ_β) and the OLD spin reordering (τ_{LD}) as a function of temperature were fitted by a power-law function $\tau = A|1 - \frac{T}{T_c}|^{-z\nu}$ (Fig. 3b), where A is the amplitude, T_c is the critical temperature, z is the dynamical critical exponent and ν is the critical exponent of the correlation length[35,36]. For comparison of the power-law scaling, the critical temperatures in each data set were adjusted to 117 K. The fitted $z\nu$ values with fitting errors are 0.95 ± 0.07 and 1.00 ± 0.04 for interlayer shear and spin reordering, respectively, in good agreement with each other. We repeated the time-resolved XRD measurements in multiple samples with different thicknesses varying from 60 to 1300 nm (Supplementary Note 5). Although the absolute relaxation time scales are thickness dependent due to different thermal cooling time scales, all the power-law fittings yield the same critical exponent $z\nu \approx 1.0$ (Supplementary Table 1), suggesting that they belong to the same universality class. In addition to the agreement of the relaxation time, the amplitude change in the interlayer shear also correlates with the OLD change upon optical excitation as a function of temperature (Fig. 3c), further confirming their strong coupling.

Similar coupled critical slowing down was observed in the recovery of the intralayer AFM order and interlayer shear along the monoclinic stacking direction in NiPS$_3$, the same direction along the zigzag AFM spin chain (Fig. 3d). The power-law fit yields $z\nu \approx 0.33$, which is different from 1.0 in FePS$_3$ because NiPS$_3$ has an XXZ-type[9] rather than the Ising-type AFM order. Using a 2D XY model, the fit for the NiPS$_3$ data yields $\nu = 0.44 \pm 0.11$ (Supplementary Fig. 8), close to the theoretical value of $\nu = 0.5$ in the model[37,38]. In contrast, the same dynamical measurements of MnPS$_3$ revealed neither interlayer shear

nor any critical slowing down across T_N (Supplementary Fig. 7). The absence of critical slowing down in MnPS$_3$ suggests the important role of interlayer shear in the formation of intralayer zigzag AFM order because MnPS$_3$ does not host the zigzag AFM order but the Néel-type Heisenberg AFM order[24].

Understanding the correlation between interlayer shear and antiferromagnetic orders

Our multimodal ultrafast probes show that the interlayer monoclinic stacking, i.e., a subtle uniaxial translational displacement between layers, is highly correlated with spin fluctuation. Close to T_N, the fluctuating intralayer AFM order prevents the recovery of interlayer shear, confirming the strong dynamical interplay of the interlayer shear and the intralayer zigzag AFM order.

To understand the coupled slowing down at T_N, we developed a phenomenological Ginzburg−Landau theory with two parameters: the magnetic order parameter denoted as η, which is related to the polarization rotation φ_{LD} as $\eta^2 \propto \varphi_{LD}$[34]; and the structural degree of freedom, denoted as $\delta\beta = \beta - \beta_{T>T_N}$, which represents the deviation of β from its high-temperature value and is linearly related to the observable $-|\Delta\beta(t)|$ with an offset. An expansion of the free energy with respect to the two parameters around T_N reads

$$F = A_\eta(T)\eta^2 + \frac{1}{2}B\eta^4 + \lambda\eta^2\delta\beta + A_\beta\delta\beta^2, \qquad (1)$$

where $A_\eta(T) = A(\frac{T}{T_N} - 1)$, A, B, A_β, and λ are constants. As shown later numerically, the linear coupling between $\delta\beta$ and η^2 is essential in the critical slowing down of the shear motion. If the coupling is of the quadratic form $\eta^2\delta\beta^2$, no coupled critical slowing down is expected. For the interlayer shear along the b axis, the shear angle is defined as the change of angle α: $\delta\alpha = \alpha - \alpha_{T>T_N}$. Because the mirror symmetry along the b axis requires $F(-\delta\alpha) = F(\delta\alpha)$, the linear coupling between $\delta\alpha$ and η^2 is forbidden. Therefore, no critical slowing down was observed in $\delta\alpha$.
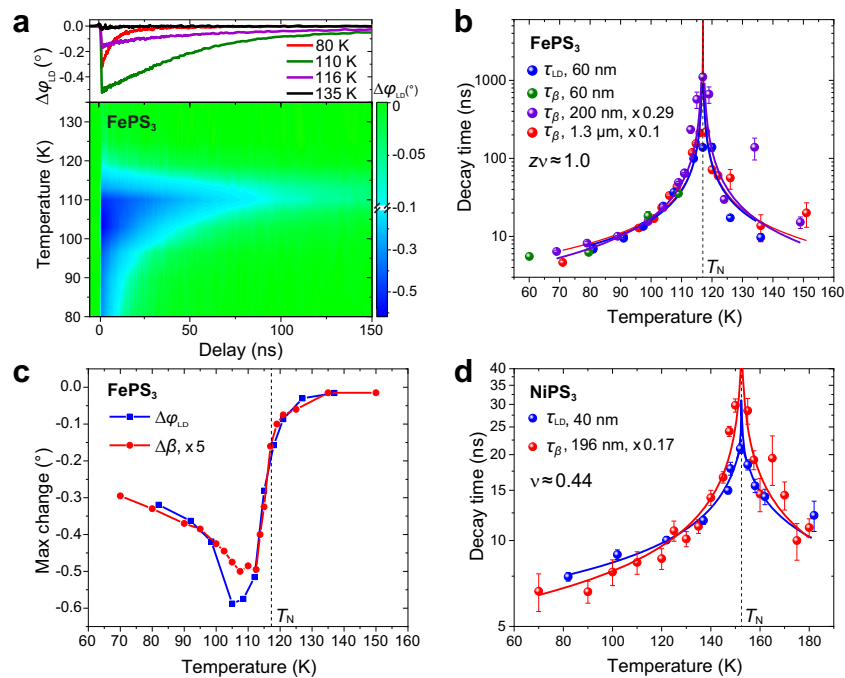
Fig. 3 | Temperature-dependent spin dynamics in *M*PS₃. a Dynamics of OLD (polarization rotation change $\Delta\varphi_{LD}$). Top panel: line cuts at four representative temperatures of the color-map plot. **b** Relaxation time of OLD and monoclinic angle β in FePS₃. The sample thickness is labeled for each dataset. **c** Comparison of $\Delta\varphi_{LD}$ and $\Delta\beta$ maximum change as a function of temperature. **d** Relaxation time of $\Delta\varphi_{LD}$ and $\Delta\beta$ in NiPS₃ (see Supplementary Fig. 7 for raw data and Supplementary Note 5 for the fitting procedure). The error bars in (**b** and **d**) represent the standard deviation of exponential fitting results (see Supplementary Note 4).

The equilibrium solutions of η and $\delta\beta$ can be obtained by minimizing the free energy F. The solutions take the form: $\eta = \pm\sqrt{2A_\eta A_\beta/(\lambda^2 - 2BA_\beta)}$ and $\delta\beta = -\lambda\eta^2/2A_\beta$ for temperature below T_N. Therefore, $\delta\beta$ is a higher-order small parameter with respect to η, and the dynamics around the Néel temperature is governed mostly by η. This correlation between $\delta\beta$ and η^2 in equilibrium is evident by comparing the measured $\delta\beta$ and φ_{LD} as a function of temperature (Fig. 4a).

As the time scale of our measurement is much longer than the periods of magnon and shear modes, the time-domain response is in an over-damped regime without oscillatory dynamics. The numerical solutions (see "Methods") of the time-dependent Ginzburg–Landau equation confirm that $\Delta\beta(t)$ follows $\Delta\varphi_{LD}(t)$ (Fig. 4b, solid lines), while no coupled critical slowing down is observed for $\delta\alpha(t)$ since it couples to $\eta^2(t)$ quadratically (Fig. 4b, red dashed lines). The scaling of the calculated relaxation time as a function of the temperature agrees with the experimental data (Fig. 4c).

The same symmetry principle also applies to NiPS₃. It exhibits a zigzag AFM order but the spins are mainly oriented within the layer (Fig. 1a), preserving the mirror symmetry with respect to the *a* axis. Therefore, similar to FePS₃, a critical slowing down should be observed in the monoclinic tilt angle β but not α, which agrees with the experimental data (Supplementary Fig. 7). If the spin orientation deviates from the *a* axis so that the mirror symmetry with respect to the *a* axis is broken, a critical slowing down in α is also expected to occur. Our theory thus provides a guidance to understanding and engineering the linear coupling between magnetic orders and lattice symmetry, distinct from the quadratic coupling modeled in three-dimensional correlated materials[39,40].

Discussion

The correlated slowing down of interlayer lattice shear and intralayer magnetic reordering clarifies their intimate relation that has been largely ignored. Although the structural change can be understood as the system accommodates the magnetic order by adjusting the lattice structures, it is interesting that these lattice degrees of freedom, *a*, *b*, *c*, α, and β, are not equivalent in their relationship with the magnetism. β shows a strong correlation with spin fluctuations because the linear term of $\eta^2\delta\beta$ survives in Eq. (1). What makes β unique is that its linear coupling to η^2 is only allowed in the monoclinic structure. The interlayer shear of the monoclinic structure breaks the intralayer three-fold rotational symmetry and becomes the primary structural degree of freedom that couples to the zigzag AFM order with the same broken rotational symmetry (Fig. 1a). As depicted in Fig. 4d, the coupled degrees of freedom jointly determine the potential energy surface. By driving the system out of equilibrium and following the relaxation pathways, the coupled parameters can be experimentally revealed. As the temperature increases close to T_N, the curvature of the energy surface is reduced, and the relaxation of coupled degrees of freedom slows down. Based on Fig. 4d, engineering the monoclinic angle away from its equilibrium value may systematically tune the free energy surface and thus influencing the magnetism. For example, decreasing monoclinic angle β can reduce η. Inversely, one expects that the magnetic order becomes stronger by increasing β, which may be an effective control scheme to increase magnetic ordering temperature in vdW materials.

The dynamical measurements using pump-probe technique can directly interrogate nonequilibrium critical phenomena because the system is driven out of equilibrium and subsequently relaxes through a wide range of nonequilibrium states before returning to its ground state. The critical exponents as obtained by fitting the scaling of the relaxation time as a function of temperature thus reflect the intrinsic fluctuations of the nonequilibrium states. The critical exponents $z\nu$ obtained through fitting the power-law scaling in FePS₃ and NiPS₃ yield distinct values of $z\nu$, 1.0 and 0.3, respectively, reflecting their intrinsic nonequilibrium magnetic fluctuations. In FePS₃, the fitting result of $z\nu = 1$ is different from the equilibrium neutron scattering measurements that fits a 2D Ising model ($z\nu = 2.1$)[41]. This discrepancy suggests that the driven fluctuations in the critical region can be different from equilibrium fluctuations but may share similarities of driven system in 3D oxides[42].
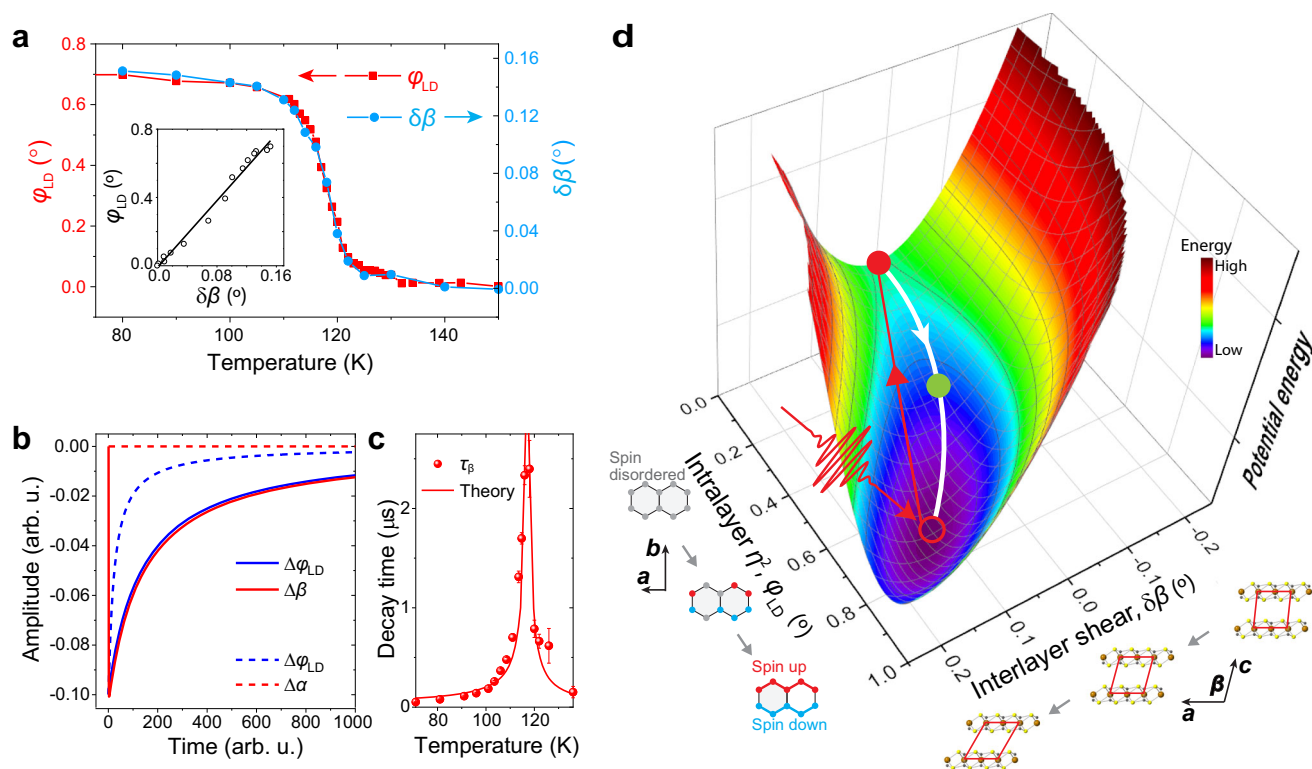
Fig. 4 | The Ginzburg–Landau model with linearly coupled structural and magnetic degrees of freedom. a Static OLD polarization rotation φ_{LD} and monoclinic angle change $\delta\beta$ in FePS$_3$ as a function of temperature. The inset shows the linear relation of these two parameters. **b** Evolution of $\Delta\varphi_{LD}$ (i.e., $\eta^2(t) - \eta^2(t<0)$), $\Delta\beta$ (i.e., $\delta\beta - 0.1°$, $0.1°$ is the β change across T_N.), and $\Delta\alpha$ close to T_N. Solid lines: coupled relaxation of $\Delta\varphi_{LD}$ and $\Delta\beta$ based on a model with a linearly coupled term ($\eta^2\delta\beta$). Dashed lines: decoupled relaxation of $\Delta\varphi_{LD}$ and $\Delta\alpha$ based on a model with a quadratically coupled term ($\eta^2\delta\alpha^2$, see "Methods"). **c** The relaxation

time of the interlayer shearing (τ_β) agrees with the numerical results based on the Ginzburg–Landau model (solid curve). **d** Schematic of the relaxation process of OLD polarization rotation and interlayer shear. The potential energy surface is generated from Eq. (1), shown as a function of intralayer magnetic order parameter and monoclinic angle. The system is excited from the ground state (open red circle) to the excited state (solid red dot) and relaxes to the ground state by a coupled recovery of magnetic order and monoclinic angle. The green solid dot represents the partially recovered intermediate state.

In summary, through quantitative measurements of critical dynamics of structural and magnetic degrees of freedom at the Néel temperature of a family of vdW antiferromagnets, we uncover the interlayer shear as the primary structural degree of freedom that couples with the intralayer magnetic order in the vdW antiferromagnets. The phenomenological model provides a framework to describe linearly coupled degrees of freedom and guiding principles for designing correlated materials and dynamical processes with large spin-mechanical effects. Our work opens a new avenue for ultrafast structural control of magnetism in all dimensions, and inversely, for spin-mediated ultrafast mechanical processes.

Methods

Sample preparation and characterization

Single-crystal MPS$_3$ bulk samples were mechanically exfoliated and transferred to sapphire substrates for XRD measurements. The OLD measurements were performed with samples on both the sapphire substrate and silicon nitride windows. The OLD results are similar with ~60 nm-thick sample on both substrates. The OLD data presented in this work are from samples on a sapphire substrate. The typical lateral size of the flakes is on the order of 100 μm. Sample thickness varies depending on individual experiments. The thickness was measured by atomic force microscopy and the thickness fringes of high-resolution XRD radial scans.

Time-resolved X-ray diffraction (XRD) experiments

The time-resolved XRD experiments were performed at the 7ID-C beamline at the Advanced Photon Source (APS). The 400 nm pump laser pulse was derived by doubling the fundamental wavelength of an

amplified Ti:Sapphire laser that outputs 100 fs laser pulse at 1 kHz repetition rate. The pump beam was incident normal to the sample with a spot size of 450 μm × 800 μm and a fluence up to 10 mJ cm^{-2}. The X-ray pulse with a duration of 100 ps and 6.5 MHz repetition rate from the synchrotron was monochromatized to an energy of 11 keV with 0.1% bandwidth and focused to a size of 20 μm (vertical) × 60 μm (horizontal) by a pair of Kirkpatrick–Baez mirrors. The sample was mounted on a six-circle diffractometer (Huber GmbH.) and cooled down by a closed-cycle helium cryostat (Advanced Research Systems). An area detector (Pilatus 100 K, DECTRIS Ltd.) was gated to selectively record the diffraction pattern from the X-ray pulses that pair with the laser excitation. The samples with various thicknesses from 60 to 1300 nm were measured. The pump fluence was adjusted so that the same thermal expansion ($\Delta c*/c* \approx 0.05\%$) was observed in samples with different thicknesses, which ensures the same optical-excitation effect regardless of the sample thicknesses.

Ultrafast optical linear dichroism (OLD) experiments

The ultrafast OLD experiments were performed at the Center for Nanoscale Materials (CNM). Asynchronous optical sampling technique was used to measure time delays up to microseconds[42]. The 400 nm, linearly polarized pump pulses were derived from a Ti: Sapphire laser with 80 fs in duration and delivered to the sample at 1 kHz repetition rate with a fluence of ~1.0 mJ cm^{-2}. The probe pulse was a white light (400 nm to 850 nm range) generated by directing 1064 nm, 80 ps pulses through a photonic crystal fiber. The 1064 nm laser pulse is the output from a laser at a repetition rate of $2 + \Delta$ kHz synchronized with the pump laser, where Δ is the detuning frequency. The probe beam was linearly polarized and oriented about 45° relative to the sample a/b

axis. The probe beam was transmitted through the sample and was split by a polarizing beam splitter into horizontal and vertical polarized beams, which were independently measured by a spectrometer with CMOS array detectors. The horizontal and vertical signals were analyzed to derive the polarization rotation angle $\Delta\varphi_{LD}$. The dynamics shown in Fig. 3a correspond to the spectrum response at 660 nm wavelength where the OLD effect reaches the maximum. A thin sample with a thickness of ~60 nm was used to allow sufficient optical transmission for detection.

Numerical calculations based on the Ginzburg–Landau theory

The time-dependent solutions of the Ginzburg–Landau equation are: $\partial\eta/\partial t = -\Gamma_\eta \partial F/\partial\eta = -2\Gamma_\eta(A_\eta\eta + B\eta^3 + \lambda\eta\delta\beta)$ and $\partial\delta\beta/\partial t = -\Gamma_\beta\partial F/\partial\delta\beta = -\Gamma_\beta(\lambda\eta^2 + 2A_\beta\delta\beta)$, where Γ_η and Γ_β are the damping rates. We first linearized the equation for $\partial\eta/\partial t$ by ignoring both the $B\eta^3$ and $\lambda\eta\delta\beta$ term. Approaching the critical temperature, $A_\eta(T) \to 0$ so that $\frac{\partial\eta}{\partial t} \to 0$. Thus $\eta^2(t)$ becomes time-invariant and exhibits a critical slowing down. Solving the equation for $\frac{\partial\delta\beta}{\partial t}$, we found $\delta\beta(t) = -\lambda\eta^2/2A_\beta + Ce^{-2A_\beta\Gamma_\beta t}$ with C being a constant. Since the second term reduces to zero quickly due to large Γ_β, $\delta\beta(t)$ follows $\eta^2(t)$ on long time scales, i.e., $\delta\beta$ also exhibits a critical slowing down. The red and blue solid lines in Fig. 4b were calculated by numerically solving the time-dependent Ginzburg–Landau equation with the following parameters: $A_\eta = 0(T = T_N)$, $B = 1.05$, $\lambda = 1.5$, $A_\beta = 1.3$, $\Gamma_\eta = 1.0$, $\Gamma_\beta = 1.3$. The red and blue dashed lines in Fig. 4b were calculated based on model: $F = A_\eta(T)\eta^2 + \frac{1}{2}B\eta^4 + \lambda\eta^2\delta\alpha^2 + A_\alpha\delta\alpha^2$, which has a quadratic order of $\delta\alpha$ in the coupling term thus results in no critical slowing down. The dashed lines were calculated based on the following parameters: $A_\eta = 0(T = T_N)$, $B = 1.05$, $\lambda = 1.5$, $A_\alpha = 1.3$, $\Gamma_\eta = 1.0$, $\Gamma_\alpha = 1.3$. For the red solid line in Fig. 4c, the parameters are the same as above except A_η, which varies between -0.05 and 0.02.

Data availability

The data plotted in the main figures are provided in the Supplementary Information/Source Data file. Additional data are available from the corresponding authors upon request. Source data are provided with this paper.

References

1. Andrei, E. Y. Graphene bilayers with a twist. *Nat. Mater.* **19**, 11 (2020).
2. Wilson, N. P., Yao, W., Shan, J. & Xu, X. Excitons and emergent quantum phenomena in stacked 2D semiconductors. *Nature* **599**, 383–392 (2021).
3. Li, J. et al. Intrinsic magnetic topological insulators in van der Waals layered $MnBi_2Te_4$ -family materials. *Sci. Adv.* **5**, eaaw5685 (2019).
4. Kang, S. et al. Coherent many-body exciton in van der Waals antiferromagnet $NiPS_3$. *Nature* **583**, 785–789 (2020).
5. Burch, K. S., Mandrus, D. & Park, J.-G. Magnetism in two-dimensional van der Waals materials. *Nature* **563**, 47–52 (2018).
6. Gong, C. & Zhang, X. Two-dimensional magnetic crystals and emergent heterostructure devices. *Science* **363**, eaav4450 (2019).
7. Gong, C. et al. Discovery of intrinsic ferromagnetism in two-dimensional van der Waals crystals. *Nature* **546**, 265–269 (2017).
8. Huang, B. et al. Layer-dependent ferromagnetism in a van der Waals crystal down to the monolayer limit. *Nature* **546**, 270–273 (2017).
9. Kim, K. et al. Suppression of magnetic ordering in XXZ-type antiferromagnetic monolayer $NiPS_3$. *Nat. Commun.* **10**, 345 (2019).
10. Gibertini, M., Koperski, M., Morpurgo, A. F. & Novoselov, K. S. Magnetic 2D materials and heterostructures. *Nat. Nanotechnol.* **14**, 408–419 (2019).
11. Deng, Y. et al. Gate-tunable room-temperature ferromagnetism in two-dimensional Fe_3GeTe_2. *Nature* **563**, 94–99 (2018).
12. Šiškins, M. et al. Magnetic and electronic phase transitions probed by nanomechanical resonators. *Nat. Commun.* **11**, 2698 (2020).
13. Jiang, S., Xie, H., Shan, J. & Mak, K. F. Exchange magnetostriction in two-dimensional antiferromagnets. *Nat. Mater.* **19**, 1295–1299 (2020).
14. Chen, W. et al. Direct observation of van der Waals stacking–dependent interlayer magnetism. *Science* **366**, 983–987 (2019).
15. Sivadas, N. et al. Stacking-dependent magnetism in bilayer CrI_3. *Nano Lett.* **18**, 7658–7664 (2018).
16. Xu, Y. et al. Coexisting ferromagnetic–antiferromagnetic state in twisted bilayer CrI_3. *Nat. Nanotechnol.* **17**, 143–147 (2022).
17. Song, T. et al. Switching 2D magnetic states via pressure tuning of layer stacking. *Nat. Mater.* **18**, 1298–1302 (2019).
18. Coak, M. J. et al. Emergent magnetic phases in pressure-tuned van der Waals antiferromagnet $FePS_3$. *Phys. Rev. X* **11**, 011024 (2021).
19. Haines, C. R. S. et al. Pressure-induced electronic and structural phase evolution in the van der Waals compound FePS 3. *Phys. Rev. Lett.* **121**, 266801 (2018).
20. Cenker, J. et al. Reversible strain-induced magnetic phase transition in a van der Waals magnet. *Nat. Nanotechnol.* **17**, 256–261 (2022).
21. Jiang, P. et al. Stacking tunable interlayer magnetism in bilayer CrI_3. *Phys. Rev. B* **99**, 144401 (2019).
22. Jang, S. W., Jeong, M. Y., Yoon, H., Ryee, S. & Han, M. J. Microscopic understanding of magnetic interactions in bilayer CrI_3. *Phys. Rev. Mater.* **3**, 031001 (2019).
23. Zhang, J., Nie, Y., Wang, X., Xia, Q. & Guo, G. Strain modulation of magnetic properties of monolayer and bilayer $FePS_3$ antiferromagnet. *J. Magn. Magn. Mater.* **525**, 167687 (2021).
24. Joy, P. A. & Vasudevan, S. Magnetism in the layered transition-metal thiophosphates MPS_3 (M = Mn, Fe, and Ni). *Phys. Rev. B* **46**, 5425–5433 (1992).
25. Lançon, D. et al. Magnetic structure and magnon dynamics of the quasi-two-dimensional antiferromagnet $FePS_3$. *Phys. Rev. B* **94**, 214407 (2016).
26. Lee, J.-U. et al. Ising-type magnetic ordering in atomically thin $FePS_3$. *Nano Lett.* **16**, 7433–7438 (2016).
27. Wang, X. et al. Raman spectroscopy of atomically thin two-dimensional magnetic iron phosphorus trisulfide ($FePS_3$) crystals. *2D Mater.* **3**, 031009 (2016).
28. Vaclavkova, D. et al. Magnon polarons in the van der Waals antiferromagnet $FePS_3$. *Phys. Rev. B* **104**, 134437 (2021).
29. Liu, S. et al. Direct observation of magnon-phonon strong coupling in two-dimensional antiferromagnet at high magnetic fields. *Phys. Rev. Lett.* **127**, 097401 (2021).
30. Sun, Z. et al. Giant nonreciprocal second-harmonic generation from antiferromagnetic bilayer CrI_3. *Nature* **572**, 497–501 (2019).
31. Guo, X. et al. Structural monoclinicity and its coupling to layered magnetism in few-layer CrI_3. *ACS Nano* **15**, 10444–10450 (2021).
32. Murayama, C. et al. Crystallographic features related to a van der Waals coupling in the layered chalcogenide $FePS_3$. *J. Appl. Phys.* **120**, 142114 (2016).
33. Zhang, X.-X. et al. Spin dynamics slowdown near the antiferromagnetic critical point in atomically thin $FePS_3$. *Nano Lett.* **21**, 5045–5052 (2021).
34. Zhang, Q. et al. Observation of giant optical linear dichroism in a zigzag antiferromagnet $FePS_3$. *Nano Lett.* **21**, 6938–6945 (2021).
35. Hohenberg, P. C. & Halperin, B. I. Theory of dynamic critical phenomena. *Rev. Mod. Phys.* **49**, 435–479 (1977).
36. Dunlavy, M. J. & Venus, D. Critical slowing down in the two-dimensional Ising model measured using ferromagnetic ultrathin films. *Phys. Rev. B* **71**, 144406 (2005).
37. Jelić, A. & Cugliandolo, L. F. Quench dynamics of the 2d *XY* model. *J. Stat. Mech.* **2011**, P02032 (2011).
38. Ramirez-Santiago, G. & José, J. V. Critical exponents of the fully frustrated two-dimensional XY model. *Phys. Rev. B* **49**, 9567–9582 (1994).

39. Yusupov, R. et al. Coherent dynamics of macroscopic electronic order through a symmetry breaking transition. *Nat. Phys.* **6**, 681–684 (2010).

40. Zhang, J. et al. Cooperative photoinduced metastable phase control in strained manganite films. *Nat. Mater.* **15**, 956–960 (2016).

41. Rule, K. C., McIntyre, G. J., Kennedy, S. J. & Hicks, T. J. Single-crystal and powder neutron diffraction experiments on $FePS_3$: search for the magnetic structure. *Phys. Rev. B* **76**, 134402 (2007).

42. Zhu, Y. et al. Unconventional slowing down of electronic recovery in photoexcited charge-ordered $La_{1/3}Sr_{2/3}FeO_3$. *Nat. Commun.* **9**, 1799 (2018).

Author contributions

F.Z., J.Z., M.Z., Y.A., D.W., A.Z., and Y.S. collected the ultrafast and static XRD data under the supervision by N.G. and H.W. F.Z., J.Z., K. H., Q.Z., and R.S. collected ultrafast optical linear dichroism data supervised by X.X and H.W. K.H. and F.Z. prepared the samples using the bulk compounds grown by Q.J. and J.H.C. C.W., L.S., and D.X. developed the theory. F.Z. and H.W. wrote the manuscript with input from all authors. H.W. conceived and supervised the project.

Competing interests

The authors declare no competing interests.

Additional information

Supplementary information The online version contains supplementary material available at https://doi.org/10.1038/s41467-022-34376-5.

Correspondence and requests for materials should be addressed to Haidan Wen.

Peer review information *Nature Communications* thanks Christian Binek and Hongjun Xian for their contribution to the peer review of this work.

Reprints and permissions information is available at http://www.nature.com/reprints

Publisher's note Springer Nature remains neutral with regard to jurisdictional claims in published maps and institutional affiliations.